DOI: 10.1002/adma.200601995

Multifunctional Nanowire Evanescent Wave Optical Sensors**

By *Donald J. Sirbuly*, *Andrea Tao*, *Matt Law*, *Rong Fan*, and *Peidong Yang**

Compact, reusable chemical sensors are highly desirable for on-site detection in the field, including the identification of water contaminants, hazardous biochemical compounds, or blood serum content. Ideally, such a sensing platform should be portable, and employ several complementary sensing modalities that allow quantitative chemical identification of extremely small sample volumes. Optical spectroscopy is a powerful analytical tool for characterizing biological and chemical systems, but making a standard optical laboratory transportable is a major challenge. However, with recent advances in the synthesis and assembly of nanomaterials,[1] it is timely to begin integrating these materials into functional device architectures for sensing and monitoring.

Of the well-studied inorganic nanostructures, chemically synthesized 1D semiconductor systems have gained significant interest from the photonics community as passive and active components for miniaturized spectroscopic devices. This is due, in part, to their ability to guide a significant portion of the confined electromagnetic energy outside the measurement cavity (i.e., in the evanescent field) while operating below the diffraction limit of light.[2] Because the evanescent field efficiently travels through fluidic and air dielectrics,[3] it is possible to integrate the waveguides into microfluidic devices and sense molecules located near the surface of the cavity. We demonstrate this by performing absorbance, fluorescence, and surface-enhanced Raman spectroscopy (SERS) measurements on sub-picoliter volumes of solution. The chemical specificity of SERS is obtained by decorating the waveguide with silver nanocubes, thus enhancing the field around the nanoribbon. Our nanowire optical sensing platform complements nanowire field-effect sensors[4] with the ability to monitor optical attenuation across the wire element. However, the use of photons instead of electrons allows optical spectroscopy to be carried out on the analyte.

Fiber-based detection is a unique alternative to free-space sensing, because it localizes chemical recognition at the surface of a waveguide. Among the most popular sensing schemes that rely on the evanescent field of a fiber are absorption[5–7] and fluorescence.[8–11] Typically, these set-ups involve multimode silica fibers with diameters much larger than the free-space wavelength of light. The evanescent field in these experiments has been used to measure refractive indices of liquids,[12] monitor volatile compounds in water,[13] and detect shifts in localized surface-plasmon resonances of coupled metal colloids.[14] Recently, the use of subwavelength silica fibers in a Mach–Zehnder-type interferometer to detect index changes caused by molecules interacting with the surface of the fibers has been proposed.[15] Although these various sensing configurations are promising for high sensitivity, fast cycling times, and reversibility, they do not provide versatility in their spectroscopic detection, nor enable a chemical read-out of the analyte. To move beyond fiber sensors that operate solely as on/off detectors it is vital to develop materials that can sustain multiple analytical modes for chemical identification.

We used single-crystalline SnO_2 nanoribbons as the passive optical components in the devices, because their high refractive indices ($n \geq 2$ for the wavelengths used here) and high aspect ratios ($>10^3$)[16] allow efficient waveguiding over extended distances in a microfluidic flow cell. In addition, their superb chemical and mechanical properties enable them to withstand harsh cleaning conditions. Figure 1 provides an overview of the poly(dimethylsiloxane) (PDMS) microfluidic devices prepared for the evanescent sensors (see Experimental section). Via micromanipulation, nanoribbons were placed across the channels in such a manner that all sides of the waveguide traversing the channel were exposed to the analyte. The final device was placed under an optical microscope (inverted, see Fig. 1C) for spectroscopic characterization while solutions were pulled through the microfluidic channels.

The first spectroscopic experiment performed with the optical waveguides was the acquisition of an absorption spectrum. This was achieved by generating the featureless defect emission on one side of the sensing channel, and collecting the light on the opposite side after it was guided through the analyte (Fig. 1B). The dye chosen for the absorption measurements was eosin-5-isothiocyanate (EITC, Molecular Probes), which is a common amine-reactive probe used to conjugate proteins or amine-modified oligonucleotides. EITC solutions

[*] Prof. P. Yang, Dr. D. J. Sirbuly,[+] A. Tao, M. Law, R. Fan
Department of Chemistry, University of California
Berkeley, CA 94720 (USA)
E-mail: p_yang@berkeley.edu
Prof. P. Yang, Dr. D. J. Sirbuly, A. Tao, M. Law, R. Fan
Materials Sciences Division, Lawrence Berkeley National Laboratory
1 Cyclotron Road, Berkeley, CA 94720 (USA)
[+] Current address: Chemistry, Materials, and Life Sciences Directorate, Lawrence Livermore National Laboratory, 7000 East Avenue, Livermore, CA 94550, USA.

[**] This work was supported in part by the Camille and Henry Dreyfus Foundation, and the Department of Energy under Contract No. DE-AC02-05CH11231. Work at the Lawrence Berkeley National Laboratory was supported by the Office of Science, Basic Energy Sciences, Division of Materials Science of the Department of Energy. Supporting Information is available online from Wiley InterScience or from the author.

ADVANCED MATERIALS

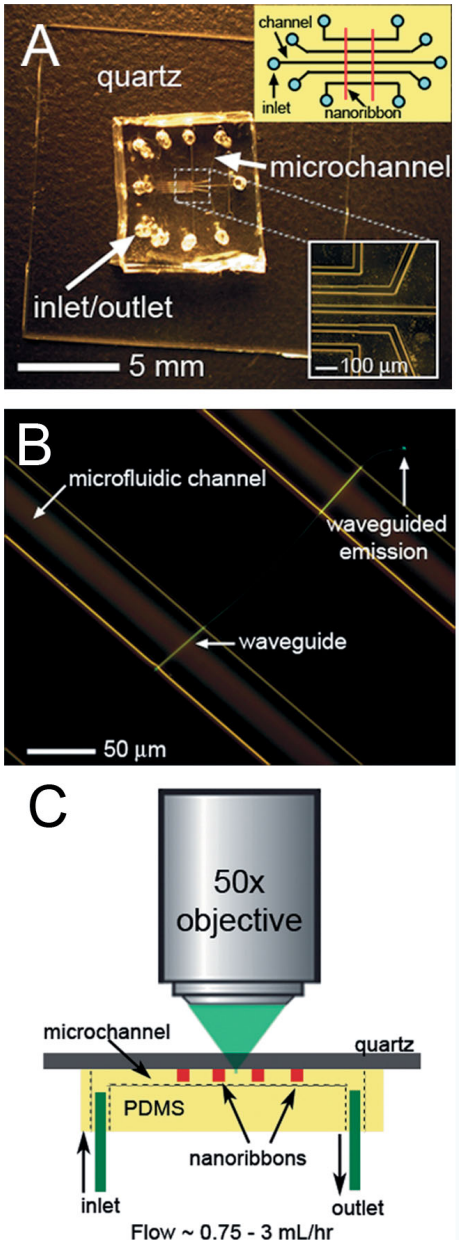

Figure 1. Device layout of the evanescent field sensors. A) Optical photograph of a device showing the polydimethylsiloxane (PDMS) microchannels and supporting quartz coverslip. Lower inset: a magnified dark-field image of the five sensing channels. Upper inset: schematic of the inlet/outlet ports and location of the waveguides. B) Dark-field/luminescence image of a single SnO_2 waveguide bridging two sensing channels. The waveguide is optically pumped outside the field of view (bottom left) and the guided emission is routed to the end facet located at the top right. C) Cartoon of the device orientation, as mounted onto the microscope.

were prepared in water (pH 12), with concentrations ranging from 0.75 to 3 mM. The solutions were pulled into the channel and sensed under continuous flow. The initial waveguided intensity (I_o) is compared to the sensing intensity (I_s) to determine the absorbance (A) of the solution according to $A = \log [I_o/I_s]$ (Fig. 2B). The attenuated fraction of I_s is directly related to the absorbance of the analyte species. The waveguides are cleaned (Fig. 2B, inset) by pulsing pure solvent (in this case pH 12 water) into the channel. The concentration dependence is linear, with a molar absorptivity (ε) of 31 000 M^{-1} cm^{-1}, which is ca. 3× lower than estimated values for EITC in 0.01 M NaOH. Although the surface of the SnO_2 nanoribbon is negatively charged at this pH (isoelectric point ca. 5) and EITC carries a net negative charge, a slight enrichment of the analyte near the waveguide/PDMS interface may occur due to van der Waals forces between the EITC molecules and the polymer. This interaction would cause a lower molar absorptivity, as seen in the EITC data. When cationic dyes, such as Rhodamine 6G, are pulled through the flow cells, multilayers form on the surface of the waveguides (see Fig. S1 in the Supporting Information).

As the SnO_2 defect emission travels through the sensing region it is attenuated according to[17]

$$I_s = I_o \exp^{-\varepsilon\kappa Lc} - I_o(NA_o^2/NA^2) \quad (1)$$

where ε is the molar absorptivity of the analyte (M^{-1} cm^{-1}), κ is the percent power in the evanescent field, L is the sensor length (cm), c is the analyte concentration, and NA and NA_o ($NA = (n_{co}^2 - n_{cl}^2)^{1/2}$) are the numerical apertures of the waveguide with and without the analyte, respectively. This is a simplified expression that neglects chemical enrichment around the SnO_2 ribbon, the shape of the cavity, and the dispersion of the field penetration; however, it gives estimates ranging from 15–30 % for the power available in the evanescent field for the waveguide dimensions used here. These results agree well with calculations describing the percent power in the core (η) of a step-index fiber,[18] which use the function

$$\eta = 1 - (5.784 \exp(-2/V)/V^3) \quad (2)$$

where $V = \pi d/\lambda(n_{co}^2 - n_{cl}^2)^{1/2}$ (d is the diameter of the fiber). For example, a 200 nm fiber ($n_{co} = 2.1$) guiding 500 nm light in water ($n_{co} = 1.33$) contains ca. 80 % of the power within the core and ca. 20 % in the evanescent field. The penetration depth (defined as the length where the field intensity decays to 10 % of the core power) is calculated to be about 125 nm, leading to a probe volume of less than 10 femtoliters for a 50 µm path length. With some simple modifications to path length, index of analyte, and cavity size, it should be possible to reach < 100 attoliter ($< 100 \times 10^{-18}$ L) probe volumes. The detection limit for absorption with a single pass through the analyte is ca. 0.3 mM, but improvements should be possible by utilizing multipass ring geometries (see Fig. S2 in the Supporting Information). Initial experiments were performed by molding ribbons into ring structures on a silica surface and placing free-standing analyte droplets on the waveguide. With this scheme, however, it is difficult to control the path length of the sensing regions due to capillary wetting of the analyte along the waveguide surface. To lower the detection limit of absorption, and control the size of the sensing region, it will be important to integrate such designs within a microfluidic flow cell.

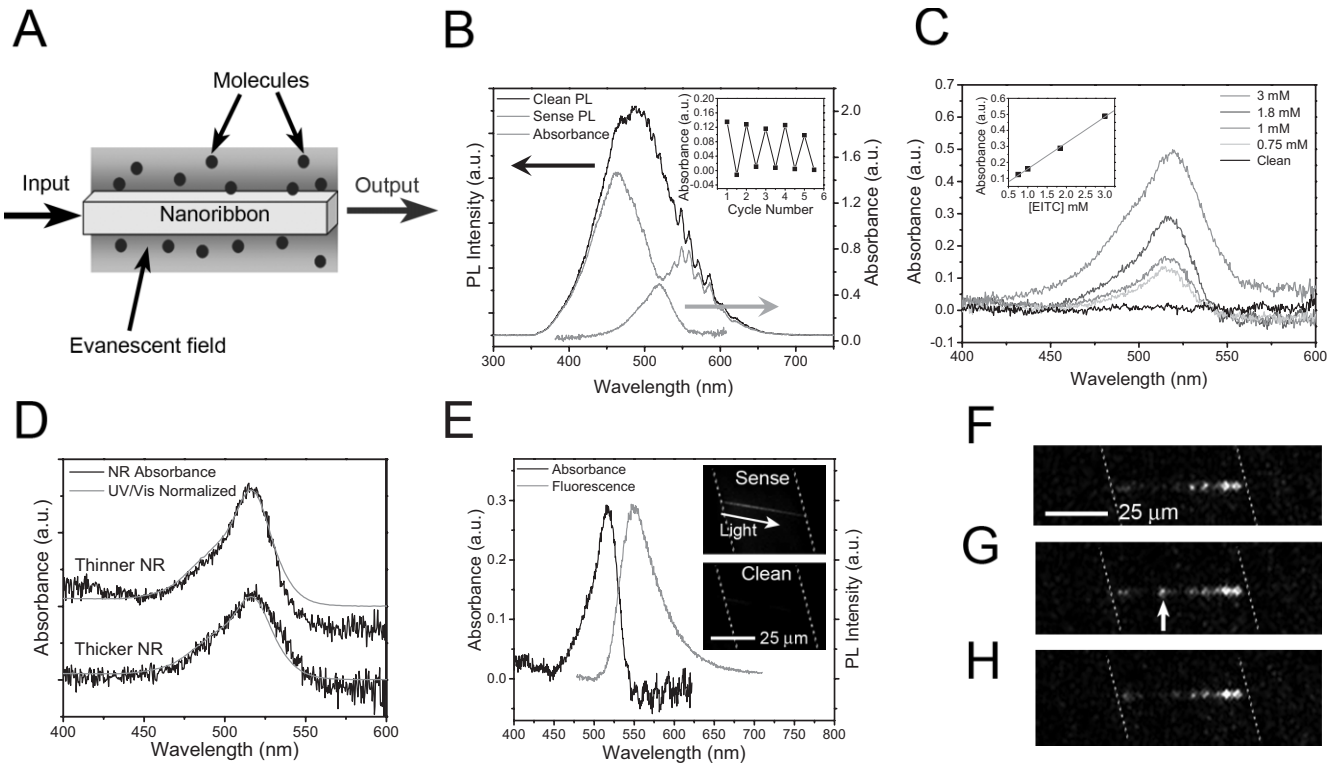

Figure 2. Use of the evanescent wave sensors in absorbance and fluorescence modes. A) Cartoon of the absorbance geometry. B) Raw waveguided fluorescence spectra before and during the flow of a 3 mM solution of EITC through a single sensing channel. The resulting absorption spectrum is shown in (C) underneath the raw spectra. Inset: cycling of the device through multiple sensing cycles, using pH 12 water to clean the waveguide. C) Absorption spectra of four EITC solutions of different concentrations. Inset: Peak absorbance versus EITC concentration showing the linear response of the sensor in this range. D) Comparison of thin ($d < 150$ nm) and thick ($d > 200$ nm) nanoribbon waveguides. The black traces are the raw waveguide absorption data and the gray traces (normalized) were taken with a conventional UV-vis spectrometer. E) Overlaid absorbance and fluorescence spectra of a 1.84 mM EITC solution using the same waveguide. Insets: photoluminescence images of a sensor in the presence of EITC (upper image) and water (lower image). F–H) A series of photoluminescence images, captured at 187 frames s^{-1} (5 ms snapshots), of λ-DNA-YOYO1 molecules flowing past a sensor. Here, 442 nm light (< 10 nW) is guided from right to left. The arrow in (G) denotes a single molecule passing through the evanescent field.

Because photons emitted near the ribbon surface can be recaptured by the waveguide, the resulting absorption line shape can be skewed. This causes an artificial decrease in the calculated absorption for longer wavelengths (Fig. 2D, top trace). We observe such an artifact only in thinner waveguides (diameters < 150 nm), which carry a larger percentage of the guided field intensity in the cladding. For thicker nanoribbons (diameters > 200 nm) the number of photons coupled back into the waveguide is reduced, but the absorption linewidth is slightly larger (Fig. 2D, bottom trace). This can be explained by the variation in penetration depth of the evanescent field as a function of the wavelength. Longer wavelengths (in this case > 525 nm) show an increase in the absorption, because they penetrate deeper into the solution. For all ribbon sizes, however, the peak maximum matches that from a commercial photospectrometer to within ca. 2 nm. More accurate peak shapes can be obtained by using expressions that account for both the amount of light accessible to the analyte at different wavelengths as well as the photon flux that is recaptured by the waveguide.

To characterize the fluorescent signals produced by the analyte, monochromatic light is launched down the cavity to excite molecules passing through the evanescent field. This mode of detection is analogous to total internal reflection fluorescence (TIRF); however, a more intense optical field resides near the core–cladding interface of a sub-200 nm nanoribbon. As with TIRF, we observe no quenching or surface effects that alter the fluorescence spectra (Fig. 2E) of the molecules excited by the evanescent field. This is often a drawback of metal-coated surfaces that can influence the spectrum of fluorophores or macromolecules, either through quenching or through effects caused by molecules adsorbing to the metal surface.[19] The fluorescence image in Figure 2E (upper inset) illustrates a typical intensity gradient along the length of a nanoribbon as 442 nm light travels through from left to right. The decay in fluorescence intensity is a result of analyte absorption as the guided light moves across the sensing channel. Less than 100 nW is confined within the core of the waveguide in this example. The signal appears linelike because the solution is too concentrated to permit single fluorophores to be distinguished. However, individual molecules can be observed if nanomolar solutions are used. This is demonstrated in the case of YOYO-1 (a nucleic acid stain) labeled λ-DNA (Fig. 2F–H). Here, portions of the waveguide appear

ADVANCED MATERIALS

to have higher concentrations of DNA near one of the edges. A likely explanation for this effect are local interactions between the DNA strands and the SnO_2 surface that cause a slight enrichment of the DNA molecules.

Light can be extracted from the waveguide by immersing particles with large dielectric constants in the evanescent field. This becomes important for ultrasensitive detection with a subwavelength fiber, because a single particle can scatter a large percentage (5–10 %) of the confined optical energy. We found that silver nanocubes with a diameter of 50 nm readily adsorbed to the waveguide surface and intensely scattered waveguided light (Fig. 3B). In general, strong scattering is observed when any particle entering the evanescent field has a larger index of refraction than the waveguide. For most waveguides used here ($d \sim 150$–200 nm), complete attenuation of the waveguided light occurred when ca. 10–15 Ag nanoparticles attached to the surface (Fig. 3B, lower image). The scattering intensity from these immobilized nanocubes can be used to quantify the index of refraction surrounding the nanoribbon. This is demonstrated in Figure 3D for three media with different refractive indices: air, $n = 1$; ethanol, $n = 1.36$; and glycol, $n = 1.43$. As expected, the scattering intensity decreases linearly with increasing index of refraction. To remove the metal nanostructures and regain the original waveguiding properties of the nanoribbon, the devices can be treated with a solution of aqua regia (1:1 HNO_3/HCl:H_2O, Fig. 3C). This allows the ribbons to be recycled by stripping them of any residual molecules or metallic contaminant.

In addition to simple index measurements, the immobilized metal particles can be utilized as substrates for SERS, where monochromatic light (532 nm was used here) from the waveguide, or from an external source, excites surface plasmons. This excitation is responsible for large increases in the Raman cross section of molecules near or adsorbed to the metal particle, allowing the collection of vibrational signatures from analytes that are undetectable with traditional Raman techniques. Resonant SERS occurs when both the analyte (in our case a dye molecule) and the metal plasmons are excited at the same wavelength. To demonstrate resonant SERS, we exposed the nanoribbons to a 100 μM solution of Rhodamine 6G ($a_{max} = 535$ nm) after decorating the waveguide surface with Ag nanocubes. The SERS signal was probed either directly, with a diffraction-limited confocal spot focused on the waveguide (Fig. 4B, SERS R6G Confocal trace), or via waveguided light (Fig. 4B, SERS R6G WG trace). In the former configuration, the waveguide acts simply as a supporting scaffold for the SERS-active particles. Here, the power at the sample is ca. 2 μW. In the latter configuration, the waveguide channels the excitation to the particles. Due to the coupling geometry the power accessible to the particles is less than 100 nW. Performing SERS with large (ca. 500 nm) and small (ca. 150 nm) diameter nanoribbons (Fig. 4B) confirms that a stronger Raman signal is achieved when a larger number of particles are scattering in the field of view. The thinner nanoribbon has about 20 nanoparticles contributing to the signal, whereas the thicker ribbon has more than 30 nanoparticles. The number of particles attached to the surface of the waveguide was quantified from charge-coupled device (CCD) images under dilute nanoparticle concentrations and slow flow rates (0.75 mL h^{-1}).

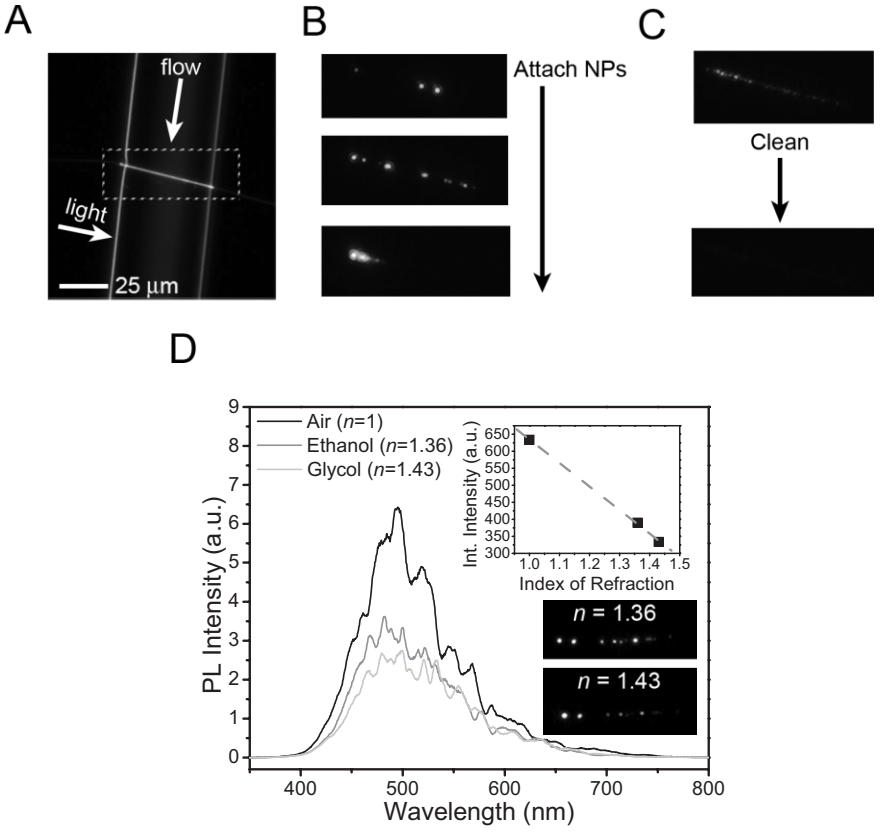

Figure 3. Dielectric scattering and refractive index sensing with silver nanoparticles. A) A dark-field image of a SnO_2 waveguide bridging a single sensing channel. The arrows denote the direction of the light and fluid flows. B) Scattering images recording Ag nanoparticles as they stick to the waveguide surface. White light is launched through the waveguide from left to right by pumping its end (outside the field of view) with 325 nm light. (from top to bottom) The time elapsed is ca. 30 s. C) Scattering images of a metal-decorated waveguide upon introduction of a 1:1 HCl/HNO_3:H_2O solution. (from top to bottom) The time elapsed is 30 s. D) Raw scattering spectra collected from the channel as various liquids flow across the waveguide. Upper inset: scattering intensity versus the index of refraction, showing the expected linear response. The inverse dependence of intensity on the index of refraction is caused by the increase in waveguide loss as the cladding index increases. Lower insets: scattering images taken from the adsorbed Ag nanoparticles in ethanol ($n = 1.36$) and glycol ($n = 1.43$).

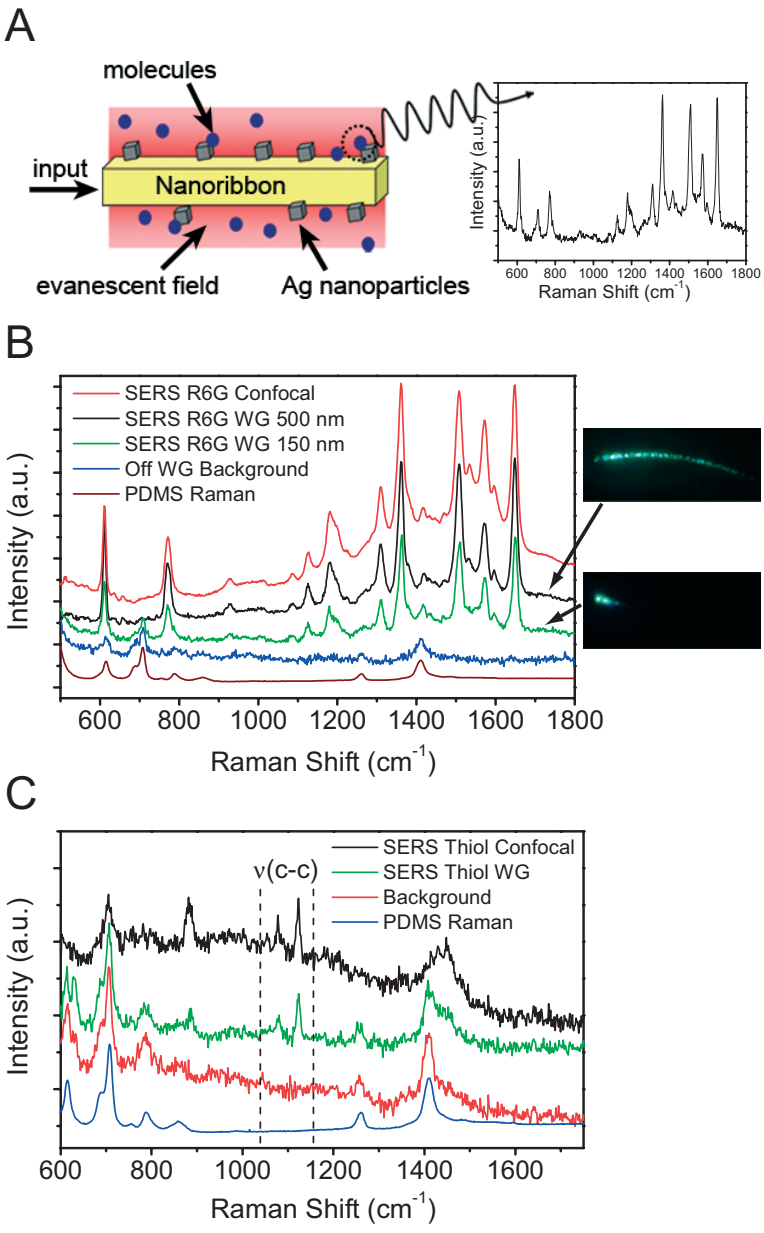

Figure 4. Nanoribbon evanescent wave SERS sensor. A) Cartoon of the sensing scheme. Analyte molecules in close proximity to a metal-decorated nanoribbon show amplified Raman scattering, which is then detected with the microscope objective. B) Resonant SERS spectra of 100 μM Rhodamine 6G. Light is delivered to the particles by direct excitation (red line) or by the evanescent field of the waveguide (SERS R6G WG traces). Large ($d \sim 500$ nm) and small ($d \sim 150$ nm) waveguides yielded identical spectra. The background (blue trace) was acquired with the beam positioned off the end facet of the waveguide. A Raman spectrum of PDMS (brown trace) verifies that the background results from PDMS. Insets: scattering images taken of the large (top) and small (bottom) waveguides. C) Nonresonant SERS of bound dodecanethiol. Direct (black) and waveguide-excited (green) SERS spectra both show the distinct C–C stretching modes of the thiol ligands at 1080 cm^{-1} and 1122 cm^{-1}. Background (red) and PDMS Raman (blue) spectra are provided for clarity.

To detect a nonresonant SERS signal from the analyte, we modified the surface of the metal with 1-dodecanethiol ligands, which readily assemble into a monolayer on the metal surface. The SERS spectra in Figure 4C clearly show the C–C stretching modes of the alkyl groups at 1080 cm^{-1} and 1122 cm^{-1} under confocal and waveguided excitation. The pump powers used were similar as described above for the Rhodamine 6G SERS. Interestingly, the signal-to-noise ratio is nearly identical for both excitation geometries, despite a lower power density for the waveguided excitation. However, the diameter of the confocal beam waist and differing number of particles in each experiment make a quantitative comparison between the two configurations difficult. Future experiments will be needed to conclude if the evanescent field scattering is a more efficient mechanism for exciting plasmons in a metallic particle attached to a subwavelength waveguide. Nevertheless, the ability to extract chemical information using a subwavelength fiber is a critical step in the development of compact analytical devices.

We have demonstrated a novel photonic sensor based on subwavelength nanowires that is capable of detecting molecules in solution by absorbance, fluorescence, and SERS. The future of portable all-optical sensors hinges on the provision of cheap, fast, and reliable detectors capable of deconvoluting complex mixtures. An imperative step in this process is the addition of chemical specificity to the sensor while simultaneously providing a multiplexed geometry for high-throughput analysis. Device portability will certainly benefit from the advent of on-chip microcavity lasers and the continual efforts of integrating both active and passive optical elements on a single photonic chip. Use of the evanescent field to guide light and perform spectroscopy will undoubtedly play a major role in the design of compact optical sensors. The initial results shown here are promising for the development of on-site analytical experimentation, field detection of biochemical toxins, and portable analysis of water contaminants.

Experimental

Tin dioxide (SnO_2) nanoribbons were synthesized through a chemical vapor transport process [20]. An alumina boat filled with tin monoxide powder was heated (1100 °C) in an alumina tube under a continuous flow of argon (300 Torr, 1 Torr = 1.333×10^2 Pa) for ca. 2 h. After removing the boat from the tube furnace, the nanoribbons were deposited on a clean glass substrate for optical characterization (see below). For SERS detection, silver nanocrystals were prepared using a modified polyol process [21] in which silver nitrate is reduced in a solution of 1,5-pentanediol (ca. 190 °C) in the presence of a capping polymer.

All experiments were performed with an upright dark-field microscope operating in reflection mode. Monochromatic laser light was focused onto the sample at a 35° angle normal to the substrate. Broadband light (full-width at half maximum (FWHM) > 200 nm) was gen-

ADVANCED MATERIALS

erated in the waveguide by exciting the SnO_2 nanoribbon with the 325 nm line of a continuous-wave HeCd laser (Melles Griot, Irvine, CA). The broad luminescence of the waveguide was used for the absorbance measurements by detecting the guided light with and without the analyte present. Fluorescence and SERS spectra were captured by focusing either a 442 (HeCd) or 532 nm (CW diode) laser spot on one of the end facets of the waveguide. Signal was collected by a 50× objective (Nikon, 0.55 numerical aperture) and routed through a fiber to a spectrometer (150 grooves/mm grating, SpectraPro 300i, Roper Scientific, Trenton, NJ) equipped with a liquid-nitrogen-cooled CCD. Images were captured either with a digital color camera (CoolSnap cf, Photometrics, Tucson, AZ) or an EMCCD camera (iXon, Andor Technology, Belfast, Northern Ireland).

Microfluidic flow cells were cast from PDMS using standard lithography. A silicon master containing 5 parallel channels (channel lengths of 1.5 mm and interchannel separation of 100 μm) was prepared with 50 μm wide × 50 μm deep channels. After casting and curing PDMS on the silicon master, the stamps were removed from the master, cleaned with ethanol, and dried. To increase exposure of the analyte to the surface area of the cavity, the waveguides were deposited in a wet PDMS layer (ca. 5 μm thick) inked on the structured side of the stamp. This also ensured complete sealing of the channels with the quartz substrate after PDMS curing and eliminated capillary leakage between adjacent channels. With the PDMS layer uncured, nanoribbons were placed across the channels using a micromanipulator (Märzhäuser Wetzlar, Wetzlar-Steindorf, Germany) equipped with an etched tungsten probe. Only ribbons with lengths greater than 350 μm were used in the devices. The stamp was then immediately bonded to a quartz substrate, giving the final device architecture shown in Figure 1A after curing the wet layer. The sharp waveguide/PDMS interfaces can be seen in Figure 1B. The optical experiments were carried out with the device oriented horizontally in the microscope with the quartz substrate facing the collection objective (Fig. 1C). Analyte solutions were pulled through the channels using a syringe pump operating at flow rates of 0.75–3 mL h^{-1}.

Unless specified, waveguides were chosen for sensing if their single-mode cut-off wavelengths were 550 nm or shorter. Waveguides were screened optically on a silica surface by pumping one of the ends of the nanoribbon with above bandgap light ($E_g = 3.6$ eV) from the HeCd laser (3.81 eV), and collecting the waveguided defect emission in the far-field at the opposite end of the ribbon. The empirical cut-off wavelength (ca. 550 nm) for the waveguides was determined by identifying the 50 % transmission point (inflection point) in the collected emission spectrum [16]. Using the waveguide parameter for a cylindrical fiber [18], the single-mode cut-off wavelength takes on the form $\lambda = d\pi/2.405(n_{co}^2 - n_{cl}^2)^{1/2}$ where d is the single-mode cut-off diameter of the waveguide and n_{co} and n_{cl} are the refractive indices of the waveguide core ($n = 2.1$) and cladding ($n = 1$), respectively. Although the nanoribbons have rectangular cross sections, we found this generalized expression gives cut-off diameters on the order of 200 nm, in good agreement ($d = 150$–200 nm) with the dimensions of the ribbons used.

Received: September 1, 2006
Published online: December 5, 2006

[1] Y. N. Xia, P. D. Yang, Y. G. Sun, Y. Y. Wu, B. Mayers, B. Gates, Y. D. Yin, F. Kim, Y. Q. Yan, *Adv. Mater.* **2003**, *15*, 353.
[2] D. J. Sirbuly, M. Law, H. Q. Yan, P. D. Yang, *J. Phys. Chem. B* **2005**, *109*, 15 190.
[3] D. J. Sirbuly, M. Law, P. Pauzauskie, H. Q. Yan, A. V. Maslov, K. Knutsen, C. Z. Ning, R. J. Saykally, P. D. Yang, *Proc. Natl. Acad. Sci. USA* **2005**, *102*, 7800.
[4] F. Patolsky, G. Zheng, O. Hayden, M. Lakadamyali, X. Zhuang, C. M. Lieber, *Proc. Natl. Acad. Sci. USA* **2004**, *101*, 14 017.
[5] V. Ruddy, B. D. Maccraith, J. A. Murphy, *J. Appl. Phys.* **1990**, *67*, 6070.
[6] M. D. DeGrandpre, L. W. Burgess, *Anal. Chem.* **1988**, *60*, 2582.
[7] Z. M. Hale, F. P. Payne, *Anal. Chim. Acta* **1994**, *293*, 49.
[8] W. H. Tan, Z. Y. Shi, S. Smith, D. Birnbaum, R. Kopelman, *Science* **1992**, *258*, 778.
[9] I. M. Walczak, W. F. Love, T. A. Cook, R. E. Slovacek, *Biosens. Bioelectron.* **1992**, *7*, 39.
[10] L. C. Shriverlake, R. A. Ogert, F. S. Ligler, *Sens. Actuators, B* **1993**, *11*, 239.
[11] A. P. Abel, M. G. Weller, G. L. Duveneck, M. Ehrat, H. M. Widmer, *Anal. Chem.* **1996**, *68*, 2905.
[12] P. Polynkin, A. Polynkin, N. Peyghambarian, M. Mansuripur, *Opt. Lett.* **2005**, *30*, 1273.
[13] D. S. Blair, L. W. Burgess, A. M. Brodsky, *Anal. Chem.* **1997**, *69*, 2238.
[14] S. F. Cheng, L. K. Chau, *Anal. Chem.* **2003**, *75*, 16.
[15] J. Y. Lou, L. M. Tong, Z. Z. Ye, *Opt. Express* **2005**, *13*, 2135.
[16] D. J. Sirbuly, M. Law, J. C. Johnson, J. Goldberger, R. J. Saykally, P. D. Yang, *Science* **2004**, *305*, 1269.
[17] M. D. DeGrandpre, L. W. Burgess, *Appl. Spectrosc.* **1990**, *44*, 273.
[18] A. W. Snyder, J. D. Love, *Optical Waveguide Theory*, Chapman and Hall, London **1983**.
[19] R. X. Bian, R. C. Dunn, S. S. Xie, P. T. Leung, *Phys. Rev. Lett.* **1995**, *75*, 4772.
[20] Z. W. Pan, Z. R. Dai, Z. L. Wang, *Science* **2001**, *291*, 1947.
[21] A. Tao, P. Sinsermsuksakul, P. Yang, *Angew. Chem. Int. Ed.* **2006**, *45*, 4579.

